Crystalline membrane morphology beyond polyhedra

Hang Yuan and Monica Olvera de la Cruz

Phys. Rev. E **100**, 012610 — Published 31 July 2019

DOI: 10.1103/PhysRevE.100.012610

Crystalline membrane morphology beyond polyhedra

Hang Yuan
Applied Physics Graduate Program, Northwestern University, Evanston, IL 60208

Monica Olvera de la Cruz*
Department of Materials Science and Engineering, Northwestern University, Evanston, IL 60208
Department of Chemistry, Northwestern University, Evanston, IL 60208 and
Department of Physics and Astronomy, Northwestern University, Evanston, IL 60208
(Dated: July 15, 2019)

Elastic crystalline membranes exhibit a buckling transition from sphere to polyhedron. However, their morphologies are restricted to convex polyhedra and are difficult to externally control. Here, we study morphological changes of closed crystalline membranes of super-paramagnetic particles. The competition of magnetic dipole-dipole interactions with the elasticity of this magnetoelastic membrane leads to concave morphologies. Interestingly, as the magnetic field strength increases, the symmetry of the buckled membrane decreases from 5-fold to 3-fold, to 2-fold and, finally, to 1-fold rotational symmetry. This gives the ability to switch the membrane morphology between convex and concave shapes with specific symmetry and provides promising applications for membrane shape control in the design of actuatable micro-containers for targeted delivery systems.

I. INTRODUCTION

Polyhedra are of great interest to scientists, mathematicians and engineers. They emerge spontaneously in many fields of science. For example, single crystals take various polyhedra shapes, fullerenes adopt beautiful truncated icosahedron shapes[1], and bacterial micro-compartments are observed in multiple regular and irregular polyhedral shapes[2].

Soft homogeneous elastic membranes, including hallow capsules[3–5], viral capsids[6, 7], elastic biological membranes[8, 9] and crystalline vesicles[10–12], can buckle under many conditions. Deformable capsules under pressure changes take on irregular shapes[13–16]. On the other hand, self-assembled crystalline membranes, like the shells of viruses, generally buckle into shapes with icosahedral symmetry[17]. These icosahedral membrane shapes have been explained by homogeneous elasticity theory[6, 18]. Furthermore, membranes with heterogeneous elasticity have been demonstrated to form various regular and irregular polyhedral shapes[19]. Such polyhedral morphologies are formed by the competition between stretching energy and bending energy. Although it is possible to engineer membrane morphologies by arranging defects in closed membrane topologies[20], these morphologies cannot go beyond polyhedra.

Here, we explore the possibility to create new closed shell morphologies, other than polyhedra, in a controllable manner. For this purpose, we consider elastic membranes of super-paramagnetic particles because of the exceptional penetration of magnetic fields and bio-compatibility. This provides opportunities to design magnetically responsive nanocarriers for targeted delivery systems in therapeutic applications[21–24]. Magnetoelastic materials form rich morphologies[25, 26] and can accomplish multimodal locomotion[27] as well as deformations that generate forces between surfaces[28] when directed by magnetic fields. The versatility of magnetoelastic filaments, which consist of super-paramagnetic particles connected by elastic linkers, has also been demonstrated experimentally[29–31] and numerically[32, 33].

Compared to magnetoelastic filaments and open membranes, closed magnetoelastic membranes, which have additional topological constraints, are found here to generate specific symmetries due to the interplay between nonlinear elasticity and magnetic dipole-dipole interactions. By using molecular dynamics simulations, we find the minimum energy configurations of magnetoelastic membranes, which can be directly controlled by external magnetic fields.

II. MODEL

As dictated by Euler's polyhedron formula, we start by triangulating a spherical shell with twelve isolated 5-fold disclinations. The disclinations are positioned on the vertices of an inscribed icosahedron (Fig. 1) to minimize the interactions between them[34], as proposed by Caspar and Klug[35].

The elastic component of the Hamiltonian of a magnetoelastic membrane, following the discretization scheme of Nelson et al[18], is written as

$$H_e = \sum_{e\in\mathbf{E}} \frac{1}{2} k \left(|\mathbf{r}_1^e - \mathbf{r}_2^e| - l_0\right)^2 + \sum_{e\in\mathbf{E}} \frac{1}{2}\tilde{\kappa}\,|\mathbf{n}_1^e - \mathbf{n}_2^e|^2 \quad (1)$$

where k is microscopic stretching constant and $\tilde{\kappa}$ is microscopic bending rigidity. The sum is over all e elements

* m-olvera@northwestern.edu

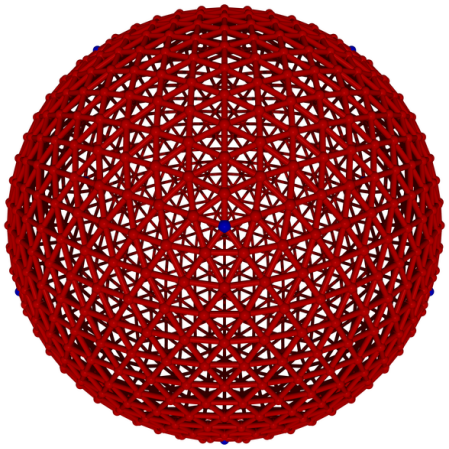

FIG. 1. Mesh configuration of the spherical shell according to Caspar and Klug construction, which is characterized by two integers h and k[35]. Above figure shows the example of $(6, 6)$ strucutre and it has 1082 vertices, 3240 edges and 2160 faces. Blue vertices correspond to the locations of 5-fold disclinations and there are 12 disclinations in total which are located on vertices of an inscribed icosahedron.

of $\mathbf{E}$, which is the set of all edges; $\mathbf{r}_1^e$ and $\mathbf{r}_2^e$ are two vertices of the edge e; and $\mathbf{n}_1^e$ and $\mathbf{n}_2^e$ are normal vectors of the two adjacent triangles of the edge e; and l_0 is the equilibrium length. Note that the corresponding continuum limit of the above discretized Hamiltonian is mesh dependent[36]. With the above described triangulation of a spherical shell, it has been shown that in the continuum limit[18, 37] Young's modulus $Y = \frac{2k}{\sqrt{3}}$, Poisson's ratio $\nu = \frac{1}{3}$ and bending rigidity $\kappa = \frac{\tilde{\kappa}}{\sqrt{3}}$.

Incompressible membranes ($\nu = 1/3$) of radius R can be described by two parameters Y and κ. Then, a single dimensionless parameter, $\gamma = \frac{YR^2}{\kappa}$, called the Föppl-von Kármán parameter[38], completely determines the buckling transition of the system. Nelson et al[6] have shown that homogeneous elastic membranes undergo a spontaneous buckling transition from sphere to icosahedron when $\gamma > \gamma^* = 154$, where 154 is the value of γ^* for a flat disk.

In our study, we place a small super-paramagnetic particle at each vertex. An external magnetic field induces a magnetic dipole on each vertex. Therefore, an additional term for magnetic dipole-dipole interactions is added into the Hamiltonian of the system:

$$H_m = -\frac{\mu_0}{4\pi} \sum_{\mathbf{r}_i, \mathbf{r}_j \in \mathbf{V}} \frac{1}{|\mathbf{r}_{ij}|^3} \left[3 \left(\boldsymbol{\mu}_i \cdot \hat{\mathbf{r}}_{ij} \right) \left(\boldsymbol{\mu}_j \cdot \hat{\mathbf{r}}_{ij} \right) - \boldsymbol{\mu}_i \cdot \boldsymbol{\mu}_j \right] \tag{2}$$

where μ_0 is the magnetic permeability in vacuum, $\boldsymbol{\mu}_i$ is the magnetic dipole moment at vertex i, $\mathbf{V}$ is the set of all vertices, $\mathbf{r}_i$ is the position vector of vertex i, $\mathbf{r}_{ij} = \mathbf{r}_j - \mathbf{r}_i$ and $\hat{\mathbf{r}}_{ij} = \mathbf{r}_{ij}/|\mathbf{r}_{ij}|$ and the sum is over $i \neq j$.

The magnetic dipole-dipole interaction is long range and anisotropic. A simplified form which considers only nearest neighbor interactions in the inextensible limit(see Appendix A) is helpful for extracting another dimensionless parameter and yields:

$$H_m \approx \left(\sum_{\mathbf{r}_i \in \mathbf{V}^{hex}} 6 + \sum_{\mathbf{r}_i \in \mathbf{V}^{pen}} 5 \right) \left({n_z^i}^2 - \frac{1}{3} \right) \tilde{M} \tag{3}$$

where $\tilde{M} = \frac{1}{4} \frac{\mu_0}{4\pi} \frac{(3\mu)^2}{l_0^3} \frac{2}{3}$, μ is the induced magnetic dipole moment which assumes only one type of super-paramagnetic particles, $\mathbf{V}^{hex}$ is the set of vertices with 6 neighbors, $\mathbf{V}^{pen}$ is the set of vertices with 5 neighbors and n_z^i is the z component of normal vector at vertex i. $\tilde{M}$ gives the characteristic energy scale for each nearest neighbor pair of magnetic dipole-dipole interactions in the discretization limit. Similar to the case of elastic membranes, a magnetic modulus can be defined in the continuum limit as $M = 8\sqrt{3}\frac{\tilde{M}}{l_0^2}$, and a dimensionless parameter, $\Gamma = \frac{MR^2}{\kappa}$, called magnetoelastic parameter[39], can be similarly defined. The magnetoelastic parameter Γ characterizes the relative strength between magnetic energy and bending energy(see Appendix B).

Therefore, the magnetoelastic membrane has one additional energy competition from magnetic dipole-dipole interactions, which is tunable via an external magnetic field. The total magnetoelastic energy of the membrane H_{em} is the sum of elastic and magnetic energies, which divided by κ gives the dimensionless form:

$$\tilde{H}_{em} \left[\{\mathbf{r}_i\}; \gamma, \Gamma \right] = \frac{H_{em}}{\kappa} = \tilde{H}_e \left[\{\mathbf{r}_i\}; \gamma \right] + \tilde{H}_m \left[\{\mathbf{r}_i\}; \Gamma \right] \tag{4}$$

where tilde indicates dimensionless quantities and note that $\tilde{H}_e$ and $\tilde{H}_m$ depend linearly on γ and Γ respectively.

Besides magnetic and elastic contributions, a volume constraint is also imposed on the membranes to account for internal pressure. This internal pressure is necessary when the membrane is not penetrable, which is modeled as:

$$H_v = \Lambda \left(\sum_k \Omega_k - V_{ref} \right)^2 \tag{5}$$

where Ω_k is the signed volume of the tetrahedron extended by k-th triangle on the membrane, V_{ref} is the reference volume of the membrane and Λ is the Lagrange multiplier which characterizes the system pressure. V_{ref} is set as volume of the icosahedron after buckling and Λ is set to a large enough value such that the membrane has additional rigidity from the volume constraint. The volume constraint is used to capture the effect from the environment surrounding the magnetoelastic membrane and eliminate possible crumpled states[40]. Corresponding cases without the volume constraint are also explored, and their morphologies generally do not differ significantly from the cases with the volume constraint. Some crumpled states and collapsed states are observed in high field strength limit for the cases

without the volume constraint(see Appendix F).

In the simulation, a shifted Lennard-Jones potential is also included for each pair of vertices to account for the exclude volume effect. Each vertex is assigned a point magnetic dipole moment. Stretching and bending are treated with a harmonic bond interaction and a harmonic dihedral interaction, respectively. Magnetic dipole-dipole interactions are calculated without a cutoff. The connectivity of the membrane is preserved during simulations. The external magnetic field is static along the z direction. We assume super-paramagnetic particles respond to an external magnetic field instantaneously and ignore rotational degrees of freedom of each vertex because super-paramagnetic particles do not have spontaneous magnetization, which decouples magnetics and elasticity. Kinetic energy is also assigned to each vertex to give a fictitious temperature of the system. The simulations start at high temperature and are gradually annealed to find the minimum energy configuration of the system. This annealing process is repeated several times to ensure that the system is not trapped in local minima (see Appendix C for more simulation details).

III. RESULTS

A collection of possible morphologies of magnetoelastic membranes obtained by systematically varying the two dimensionless parameters, the Föppl-von Kármán parameter γ and the magnetoelastic parameter Γ, are shown in Fig. 2 (For a more detailed shape diagram, please refer to Fig. 4). Without magnetic dipole-dipole interactions (Γ=0), when $\gamma < \gamma^*$, the homogeneous elastic crystalline membrane tends to stay spherical (Fig. 2a) and when $\gamma > \gamma^*$ it buckles into an icosahedron (Fig. 2b) as expected in the conventional homogeneous elastic crystalline membranes[6].

At moderate strengths of the magnetic dipole-dipole interaction, as shown in the second row of Fig. 2, the structures deform since the magnetic dipoles prefer to line up and stay closer to each other to minimize the magnetic energy. When the membrane is relatively soft ($\gamma < \gamma^*$), the membrane tends to elongate along the direction of the external magnetic field. However, this is opposed by elastic interactions since elasticity prefers the membrane to stay spherical, resulting in an ellipsoid like membrane morphology as shown in Fig. 2c.

When the membrane is relatively stiff ($\gamma > \gamma^*$), the membrane undergoes an elastically driven buckling transition. The interplay between nonlinear elasticity and magnetic dipole-dipole interactions distorts the icosahedron. The flat regions of the icosahedron bend inward to reduce the distance between magnetic dipoles and disclinations pair up, resulting in a star-like morphology with six ridges as shown in Fig. 2d. Unlike the conventional convex polyhedral morphologies of the purely elastic membranes, the magnetoelastic membranes develop concave regions.

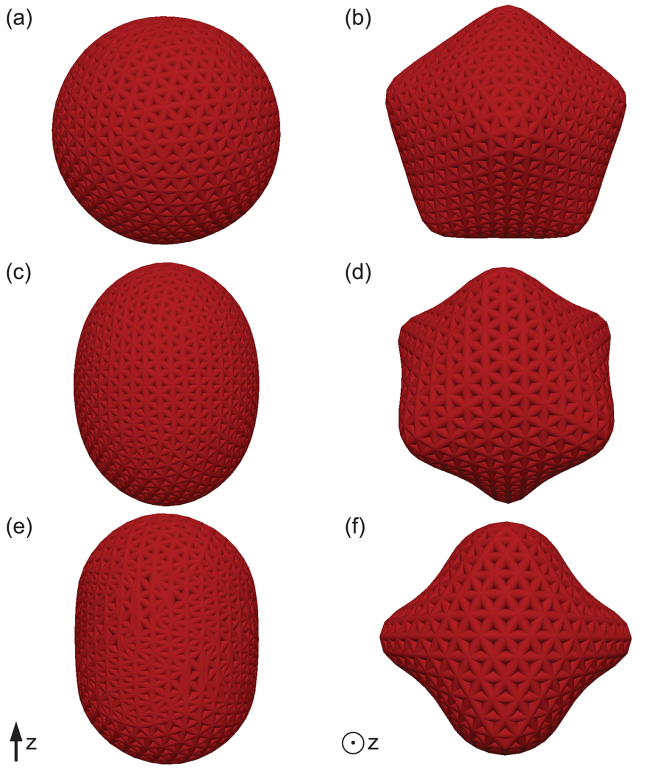

FIG. 2. A collection of representative minimum energy morphologies of closed magnetoelastic membranes with different parameters pair (γ, Γ): Föppl-von Kármán parameter γ and magnetoelastic parameter Γ; γ increases from left to right and Γ increases from top to bottom. (a) spherical shape (100,0); (b) icosahedral shape (1000,0); (c) ellipsoidal shape (100,25); (d) star shape with six ridges (1000,100); (e) cylindrical shape (100,50); (f) star shape with four ridges (1000,200). Note that first column is shown from y-direction and second column is shown from z-direction to give better illustration of morphologies. Arrows indicate the direction of the external magnetic field. Please see SM1 - 6 for corresponding animated membrane morphologies.

Then, consider the case of strong magnetic dipole-dipole interactions, as shown in the third row of Fig. 2. The elastic energy becomes comparable with the magnetic energy until the membrane is highly deformed. In this regime, the competition between magnetic energy and elastic energy results in another new family of morphologies.

When the membrane is easily deformed ($\gamma < \gamma^*$), magnetic dipole-dipole interactions tend to elongate the membrane further along the direction of the external magnetic field in this high field strength regime. However, the elastic energy can no longer hold the membrane in a spherical or ellipsoidal shape. The membrane forms a cylindrical shape, as shown in Fig. 2e, to minimize the magnetic energy. Although the bending energy is high along edges of two end caps of the cylinder, the total energy decreases by lining up vertices on the side surface

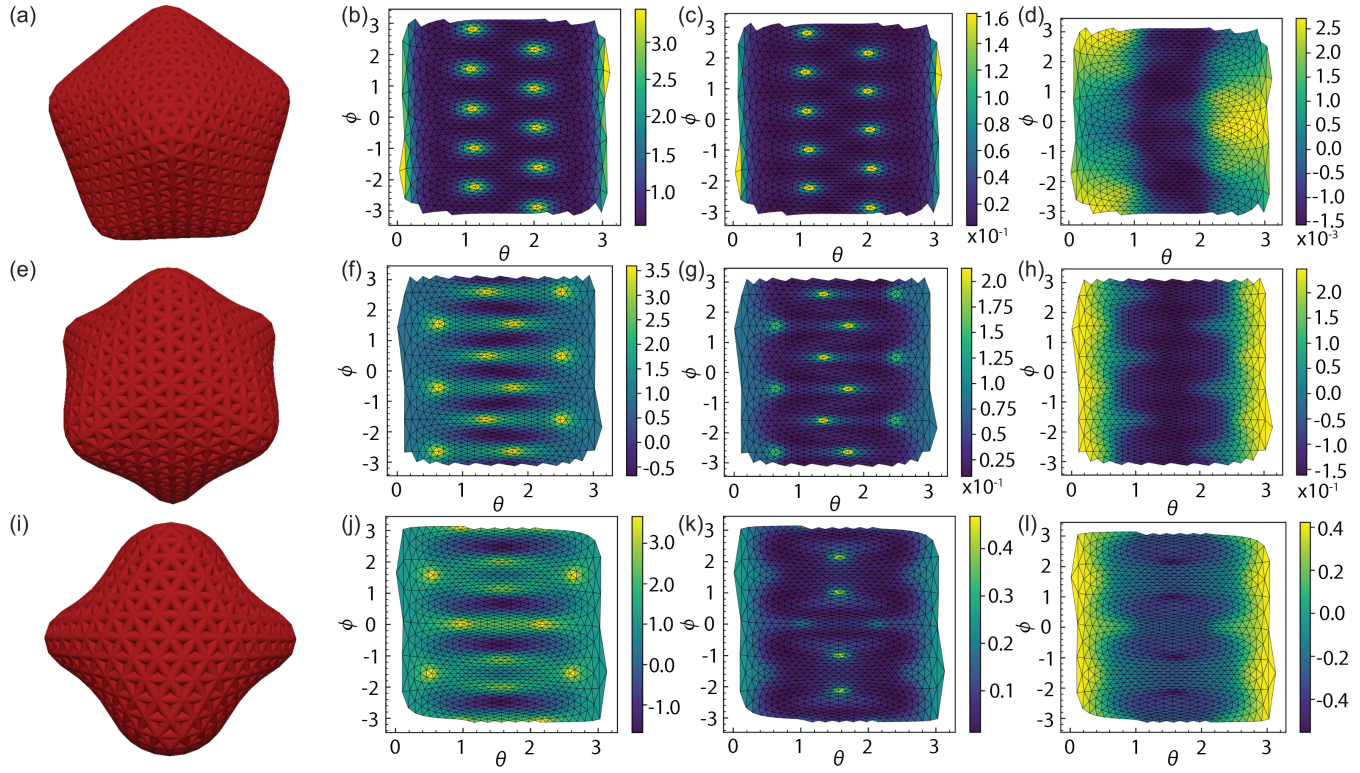

FIG. 3. membrane morphologies(first column), mean curvature distribution(second column), elastic energy distribution(third column) and magnetic energy distribution(fourth column) showing symmetry of magnetoelastic membranes. Membrane morphologies in the first column are shown from z-direction. All other plots are shown in spherical coordinates. Horizontal axis is polar angle $\theta \in [0, \pi]$ and vertical axis is azimuthal angle $\phi \in (-\pi, \pi]$. Mean curvatures are chose to be signed values where positive values indicate convex regions and negative values indicate concave regions. Elastic energy is sum of stretching energy(bond interaction) and bending energy(dihedral interaction). Magnetic energy is sum of magnetic dipole-dipole interactions. Energy from Lennard-Jones interactions is negligible in all three cases. Parameters pairs (γ, Γ) of membranes in each row are: (1000,1), (1000,100), (1000,200) from top to bottom.

of the cylinder.

When the membrane is relatively rigid ($\gamma > \gamma^*$), the elastic energy tries to preserve the total surface area of the membrane since stretching is much more expensive than bending in this case. Meanwhile, the magnetic dipole-dipole interaction tries to reduce the total volume of the membrane to minimize the magnetic energy. This competition, combined with the nonlinearity introduced by the twelve disclinations, results in a star-like morphology with four ridges as shown in Fig. 2f. Note that the membrane in this case is highly bent inward, which reduces its total volume significantly and opens some possible applications as discussed later.

Among all these mentioned morphologies of the magnetoelastic membrane, the $\gamma \sim 1000$ cases are particularly interesting because this regime corresponds to a typical Föppl-von Kármán parameter of viral shells[6]. In this regime, where both nonlinear elasticity and magnetic dipole-dipole interactions can be significant, we find that the magnetoelastic membrane tends to choose configurations that decrease symmetry with increasing external magnetic field strength. This point is illustrated by plotting the mean curvature and energy distribution of the membrane in spherical coordinates as shown in Fig. 3.

In the weak field strength limit, the membrane forms an icosahedron (Fig. 3a) with five-fold rotational symmetry around the z-axis as shown in Fig. 3b and 3c. In this limit, the elastic energy dominates and the magnetic energy is negligible (Fig. 3d). With a moderate external magnetic field strength, the membrane morphology has six ridges(Fig. 3e). However, the 12 isolated disclinations prefer to pair up and form ridges connecting each pair of disclinations[41]. These disclinations pairs are arranged alternatively to maximize the mutual distance in order to reduce interactions between disclinations[34] and ridges[42], as shown in Fig. 3f and 3g. Because of this alternative arrangement, the membrane with six ridges has only three-fold rotational symmetry around the z-axis, which is also reflected by the magnetic energy distribution (Fig. 3h). If the field strength is further increased, the membrane starts to form morphologies with four ridges (Fig. 3i). In this regime, two pairs of disclinations break and there is a single disclination near each of the four concave regions as show in Fig. 3j and 3k. Therefore, the symmetry of the membrane reduces

to two-fold rotational symmetry (Fig. 3j, 3k and 3l) around the z-axis. In the extremely high field strengths regime, the magnetic energy completely dominates and the membrane collapses and takes one-fold rotational symmetry(the collapsed state is not shown in Fig. 3).

A natural question is to ask why the four-fold rotational symmetry is missing among all these above mentioned morphologies. This is due to two important facts: the ridges connecting each pair of disclinations are energetically expensive to break up[43] and there are effective repulsive interactions between disclinations[34] and ridges[42]. The existence of four-fold symmetric structures requires that 12 disclinations are divided into 4 groups of 3 disclinations, which needs strong enough external magnetic field strength to break up the ridge structures. Even these 4 groups of 3 disclinations are formed, four-fold symmetric structures are still not energetically favorable since the total energy of the system can be further reduced by choosing an alternative arrangement to increase mutual distances and reduce repulsive interactions between disclinations and ridges. This alternative arrangement brings the system directly into two-fold symmetric structures, which makes four-fold symmetric structures are never observed as a lowest energy configuration in our simulations.

When the volume constraint is removed, we find similar morphologies to those discussed above except in high magnetic field strengths, where they take on crumpled or collapsed morphologies (see Fig. 6).

IV. CONCLUSIONS

In summary, crystalline magnetoelastic membranes exhibit concave morphologies beyond the conventional polyhedral shapes found in elastic membranes. Magnetic dipole-dipole interactions give an additional control parameter which is the magnetoelastic parameter Γ. Combining with the Föppl-von Kármán parameter γ in the elastic membranes, these two dimensionless parameters provide guidelines for analyzing properties of crystalline magnetoelastic membranes. Importantly, since γ is hard to change once a membrane is assembled, the magnetoelastic parameter, which can be easily manipulated by an external magnetic field, provides a way to tune the membrane morphology between convex shapes and concave shapes with specific symmetry.

Exciting applications, including reversible membrane shape control, design of micro-containers, and targeted drug delivery, are expected for the closed crystalline magnetoelastic membranes. For example, since the volume to surface ratio of magnetoelastic membranes can be highly reduced by imposing an external magnetic field, the concentration inside can be much higher than that in the outside environment. This morphological change induced by the external magnetic field can facilitate release of cargoes. Therefore, the magnetoelastic membrane can be used as a container to carry and protect volatile or toxic molecules and release them in a targeted region labelled by the external magnetic fields.

ACKNOWLEDGMENTS

This work was supported as part of the Center for Bio-Inspired Energy Science, an Energy Frontier Research Center funded by the US Department of Energy, Office of Science, Basic Energy Sciences under Award DE-SC0000989.

Appendix A: Approximate magnetic energy expression

Compared to the conventional elastic membranes, the energy of magnetoelastic membranes has an additional contribution from magnetic dipole-dipole interactions, which can be expressed as:

$$H_m = -\frac{\mu_0}{4\pi} \sum_{\mathbf{r}_i,\mathbf{r}_j \in \mathbf{V}, i\neq j} \frac{1}{|\mathbf{r}_{ij}|^3} \left[3\left(\boldsymbol{\mu}_i \cdot \hat{\mathbf{r}}_{ij}\right)\left(\boldsymbol{\mu}_j \cdot \hat{\mathbf{r}}_{ij}\right) - \boldsymbol{\mu}_i \cdot \boldsymbol{\mu}_j\right] \tag{A1}$$

where μ_0 is the magnetic permeability in vaccum, $\boldsymbol{\mu}_i$ is the magnetic dipole moment at vertex i, $\mathbf{V}$ is the set of all vertices, $\mathbf{r}_i$ is the position vector of vertex i, $\mathbf{r}_{ij} = \mathbf{r}_j - \mathbf{r}_i$ and $\hat{\mathbf{r}}_{ij} = \mathbf{r}_{ij}/|\mathbf{r}_{ij}|$.

We further assume the magnetic filed strength is strong enough that the induced magnetic dipole of each super-paramagnetic particles always aligns with the external magnetic field. For simplicity, we only consider the case where a magnetoelastic membrane is composed of the same type of super-paramagnetic particles. Then, the induced magnetic dipole moments of each super-paramagnetic particles are the same: $\boldsymbol{\mu}_i = \boldsymbol{\mu} = \mu\hat{\mathbf{m}}$, where $\hat{\mathbf{m}}$ is the direction of the external magnetic field.

The above magnetic dipole-dipole interactions term can be simplified by including only nearest neighbor interactions:

$$\begin{aligned} H_m &\approx -\frac{\mu_0}{4\pi} \sum_{\mathbf{r}_i,\mathbf{r}_j \in \mathbf{V}, i\neq j} \frac{1}{|\mathbf{r}_{ij}|^3} \left[3\left(\boldsymbol{\mu} \cdot \hat{\mathbf{r}}_{ij}\right)^2 - \mu^2\right] \\ &\approx -\frac{\mu_0}{4\pi} \sum_{\mathbf{r}_i \in \mathbf{V}} \sum_{\mathbf{r}_j \in \text{neighbors of i}} \frac{1}{|\mathbf{r}_{ij}|^3} \left[3\left(\boldsymbol{\mu} \cdot \hat{\mathbf{r}}_{ij}\right)^2 - \mu^2\right] \\ &= \frac{\mu_0 \mu^2}{4\pi} \sum_{\mathbf{r}_i \in \mathbf{V}} \sum_{\mathbf{r}_j \in \text{neighbors of i}} \frac{1}{|\mathbf{r}_{ij}|^3} \left[1 - 3\left(\hat{\mathbf{m}} \cdot \hat{\mathbf{r}}_{ij}\right)^2\right] \end{aligned} \tag{A2}$$

Furthermore, we assume the membrane is inextensible, which means that the stretching constant is large enough and thus all edge lengths are close to the equilibrium length l_0. With this assumption, all vertices are roughly equally distant and there are only two types of vertices: vertices with five neighbors(five-fold disclinations) and vertices with six neighbors. Thus, the magnetic energy

associated with each vertex type can be calculated accordingly:

1. Hexagonal vertex
   In this case, the vertices have six neighbors which locate on vertices of a regular hexagon. Assuming the equilibrium length l_0 is small enough that locally six neighbors are in the same plane. By choosing z-axis as the normal direction of this regular hexagon(moving frame), locations of six neighbors can be written as $\hat{\mathbf{r}}_j = \left(\cos\frac{j\pi}{3}, \sin\frac{j\pi}{3}, 0\right), j = 0, \cdots, 5$ and the direction of the external magnetic field in this coordinate system can be expressed as $\hat{\mathbf{m}} = \left(r_t^i \cos\theta_t^i, r_t^i \sin\theta_t^i, m_n^i\right)$, where r_t^i is the magnitude of in-plane component of $\hat{\mathbf{m}}$ at vertex i, θ_t^i is the corresponding polar angle in the plane and m_n^i is the magnitude of out-plane component of $\hat{\mathbf{m}}$ at vertex i. Note that the components of $\hat{\mathbf{m}}$ in the chosen coordinate system depend on the location of vertex i. Then, the magnetic energy associated with each hexagonal vertex is

$$\begin{aligned}\epsilon_{hex}^i &= \frac{\mu_0\mu^2}{4\pi} \sum_{j\in\text{neighbors of i}} \frac{1}{|\mathbf{r}_{ij}|^3}\left[1 - 3\left(\hat{\mathbf{m}}\cdot\hat{\mathbf{r}}_{ij}\right)^2\right] \\ &= \frac{\mu_0\mu^2}{4\pi}\sum_{j=0}^{5}\frac{1}{l_0^3}\left[1 - 3{r_t^i}^2\cos^2\left(\theta_t^i - \frac{j\pi}{3}\right)\right] \\ &= \frac{\mu_0\mu^2}{4\pi}\frac{6}{l_0^3}\left[1 - \frac{3}{2}{r_t^i}^2\right]\end{aligned} \tag{A3}$$

2. Pentagonal vertex
   By similarly choosing the coordinate system, the locations of neighbor vertices in the pentagonal case can be written as $\hat{\mathbf{r}}_j = \left(\cos\frac{2j\pi}{5}, \sin\frac{2j\pi}{5}, 0\right), j = 0, \cdots, 4$. The magnetic energy associated with each of the disclination vertices is:

$$\begin{aligned}\epsilon_{pen}^i &= \frac{\mu_0\mu^2}{4\pi} \sum_{j\in\text{neighbors of i}} \frac{1}{|\mathbf{r}_{ij}|^3}\left[1 - 3\left(\hat{\mathbf{m}}\cdot\hat{\mathbf{r}}_{ij}\right)^2\right] \\ &= \frac{\mu_0\mu^2}{4\pi}\sum_{j=0}^{4}\frac{1}{l_0^3}\left[1 - 3{r_t^i}^2\cos^2\left(\theta_t^i - \frac{2j\pi}{5}\right)\right] \\ &= \frac{\mu_0\mu^2}{4\pi}\frac{5}{l_0^3}\left[1 - \frac{3}{2}{r_t^i}^2\right]\end{aligned} \tag{A4}$$

We consider a static external magnetic field pointing along the z-direction. Then, the direction of the external magnetic field is $\hat{\mathbf{m}} = (0, 0, 1)$ in the lab coordinate system. Denote the normal vector of i-th vertex as $\mathbf{n}_i$ and it can be expressed as $\hat{\mathbf{n}}_i = (n_x^i, n_y^i, n_z^i)$ in the lab coordinate system. Thus, the in-plane component of $\hat{\mathbf{m}}$ at each vertex i is:

$${r_t^i}^2 = [\hat{\mathbf{m}} - (\hat{\mathbf{m}}\cdot\hat{\mathbf{n}}_i)\hat{\mathbf{n}}_i]^2 = 1 - (\hat{\mathbf{m}}\cdot\hat{\mathbf{n}}_i)^2 = 1 - {n_z^i}^2 \tag{A5}$$

Plugging the above expression back into the energy expressions of the hexagonal vertex and the pentagonal vertex, we get

$$\epsilon_{hex}^i = 6\tilde{M}\left({n_z^i}^2 - \frac{1}{3}\right) \tag{A6}$$

$$\epsilon_{pen}^i = 5\tilde{M}\left({n_z^i}^2 - \frac{1}{3}\right) \tag{A7}$$

where $\tilde{M}$ gives the characteristic dipole-dipole interaction strength between a pair of nearest neighbors and is defined as:

$$\tilde{M} = \frac{1}{4}\frac{\mu_0}{4\pi}\frac{(3\mu)^2}{l_0^3}\frac{2}{3} \tag{A8}$$

Then, putting all parts together gives the total magnetic energy of the membrane with the nearest neighbor approximation in the inextensible limit:

$$H_m \approx \left(\sum_{\mathbf{r}_i\in\mathbf{V}^{hex}} 6 + \sum_{\mathbf{r}_i\in\mathbf{V}^{pen}} 5\right)\tilde{M}\left({n_z^i}^2 - \frac{1}{3}\right) \tag{A9}$$

We can bring the above discretization limit expression into the continuum limit by associating each vertex with its Voronoi cell area. The area of a regular hexagon with edge length l_0 is $\frac{3\sqrt{3}}{2}l_0^2$ and the corresponding Voronoi cell area of hexagonal vertex is $\frac{\sqrt{3}}{2}l_0^2$. Then, the magnetic energy density in the continuum limit is:

$$\epsilon_M = \frac{\epsilon_{hex}}{\frac{\sqrt{3}}{2}l_0^2} = \frac{1}{2}M\left(n_z^2 - \frac{1}{3}\right) \tag{A10}$$

where the magnetic modulus M is defined as

$$M = 2\sqrt{3}\frac{\mu_0}{4\pi l_0}\left(\frac{3\mu}{l_0^2}\right)^2\frac{2}{3} \tag{A11}$$

Note that the above magnetic modulus has an addition factor of $2\sqrt{3}$ comparing with the result derived for square mesh[39]. The total magnetic energy in the continuum limit can be expressed as an integral of the magnetic energy density:

$$H_m \approx \int \frac{1}{2}M\left(n_z^2 - \frac{1}{3}\right)\mathrm{d}S \tag{A12}$$

Appendix B: Dimensionless parameters

The total magnetoelastic energy of the membrane in the discretization limit can be expressed as:

$$\begin{aligned} H_{em} &= \sum_{e\in\mathbf{E}} \frac{1}{2}k\left(|\mathbf{r}_1^e-\mathbf{r}_2^e|-l_0\right)^2 + \sum_{e\in\mathbf{E}} \frac{1}{2}\tilde{\kappa}\left|\mathbf{n}_1^e-\mathbf{n}_2^e\right|^2 \\ &- \frac{\mu_0}{4\pi}\sum_{\mathbf{r}_i,\mathbf{r}_j\in\mathbf{V},i\neq j}\frac{1}{|\mathbf{r}_{ij}|^3}\left[3\left(\boldsymbol{\mu}_i\cdot\hat{\mathbf{r}}_{ij}\right)\left(\boldsymbol{\mu}_j\cdot\hat{\mathbf{r}}_{ij}\right)-\boldsymbol{\mu}_i\cdot\boldsymbol{\mu}_j\right] \\ &\approx \sum_{e\in\mathbf{E}} \frac{1}{2}k\left(|\mathbf{r}_1^e-\mathbf{r}_2^e|-l_0\right)^2 + \sum_{e\in\mathbf{E}} \frac{1}{2}\tilde{\kappa}\left|\mathbf{n}_1^e-\mathbf{n}_2^e\right|^2 \\ &+ \left(\sum_{\mathbf{r}_i\in V^{hex}} 6 + \sum_{\mathbf{r}_i\in\mathbf{V}^{pen}} 5\right)\tilde{M}\left({n_z^i}^2-\frac{1}{3}\right) \end{aligned} \tag{B1}$$

where k is the microscopic stretching constant, $\tilde{\kappa}$ is the microscopic bending constant and $\tilde{M}$ is the microscopic characteristic dipole-dipole interaction strength. By choosing the unit energy as $\tilde{\kappa}$ and the unit length as R (radius of the initial spherical shell), the above expression becomes dimensionless:

$$\begin{aligned} \tilde{H}_{em} &= \sum_{e\in\mathbf{E}} \frac{1}{2}\frac{kR^2}{\tilde{\kappa}}\left(\left|\tilde{\mathbf{r}}_1^e-\tilde{\mathbf{r}}_2^e\right|-\tilde{l_0}\right)^2 + \sum_{e\in\mathbf{E}} \frac{1}{2}\left|\mathbf{n}_1^e-\mathbf{n}_2^e\right|^2 \\ &+ \left(\sum_{\mathbf{r}_i\in V^{hex}} 6 + \sum_{\mathbf{r}_i\in\mathbf{V}^{pen}} 5\right)\frac{\tilde{M}}{\tilde{\kappa}}\left({n_z^i}^2-\frac{1}{3}\right) \\ &= \sum_{e\in\mathbf{E}} \frac{1}{2}\tilde{\gamma}\left(\left|\tilde{\mathbf{r}}_1^e-\tilde{\mathbf{r}}_2^e\right|-\tilde{l_0}\right)^2 + \sum_{e\in\mathbf{E}} \frac{1}{2}\left|\mathbf{n}_1^e-\mathbf{n}_2^e\right|^2 \\ &+ \left(\sum_{\mathbf{r}_i\in V^{hex}} 6 + \sum_{\mathbf{r}_i\in\mathbf{V}^{pen}} 5\right)\tilde{\Gamma}\left({n_z^i}^2-\frac{1}{3}\right) \end{aligned} \tag{B2}$$

Note that the above Hamiltonian has two dimensionless parameters $\tilde{\gamma}=\frac{kR^2}{\tilde{\kappa}}$ and $\tilde{\Gamma}=\frac{\tilde{M}}{\tilde{\kappa}}$, which give characteristic interaction strengths in the microscopic scale. We can also bring the system into the continuum limit, which gives two more familiar dimensionless parameters of the system:

$$\gamma=\frac{YR^2}{\kappa}, \Gamma=\frac{MR^2}{\kappa} \tag{B3}$$

where γ is the Föppl-von Kármán parameter, which gives characteristic relative strength between stretching interaction and bending interaction. Γ is the magnetoelastic parameter, which gives characteristic relative strength between magnetic dipole-dipole interaction and bending interaction. Also note that $\Gamma\propto\mu^2$ and induced magnetic dipole moment μ is proportional to the strength of external magnetic field, which means that Γ can be directly controlled by an external magnetic field. Correspondences between parameters in the discretization limit and the continuum limit[18, 37] are listed below:

$$Y=\frac{2k}{\sqrt{3}}, \kappa=\frac{\tilde{\kappa}}{\sqrt{3}}, M=\frac{8\sqrt{3}}{l_0^2}\tilde{M} \tag{B4}$$

Appendix C: Details of simulation setup

The simulations are performed in LAMMPS[44]. All interactions in the Hamiltonian of the system can be mapped to commonly available interactions in LAMMPS. More specifically, stretching interactions are modeled as harmonic bond interactions, bending interactions are modeled as harmonic dihedral interactions, and magnetic dipole-dipole interactions are modeled as electric dipole-dipole interactions (both are equivalent in reduced units). Shifted Lennard-Jones interactions are included to account for finite size effect of the super-paramagnetic particles and to increase the stability of the collapsed state simulation. The cutoff of the Lennard-Jones interactions is set as 0.6 of equilibrium length l_0. The equilibrium length l_0 is set as the average bond length of the initial mesh.

Each vertex is represented as a point dipole in the simulations. The computation of the long range magnetic dipole-dipole interactions is performed using the long range solver PPPM/dipole in LAMMPS. Because of properties of super-paramagnetic particles, directions of each dipole are always aligned with the external magnetic field. Besides, only translational degrees of freedom are updated in each timestep. Rotational degrees of freedom of each vertex are ignored because super-paramagnetic particles don't have permanent magnetization which decouples magnetics and elasticity.

Initial mesh of the membrane is constructed with the scheme proposed by Caspar and Klug[35]. Different mesh choices (different h,k numbers) are tested to ensure that the observed phenomena are not mesh dependent. All simulations mentioned in this paper are performed with mesh $(6,6)$, which has 1082 vertices, 3240 edges and 2160 faces. We use reduced units for all simulations; the unit energy is $\tilde{\kappa}$ and the unit length is R (radius of initial mesh). By choosing a different stretching constant for harmonic bond interactions(k) and the induced magnetic dipole moment(μ), all possible dimensionless parameters pair (γ,Γ) can be constructed accordingly.

The simulations are performed with a typical annealing process to get the minimum energy configuration of the magnetoelastic membranes. The annealing process is repeated five times to ensure the final membrane configuration is not trapped in local minima.

The volume constraint is added when the membrane is not penetrable, which is implemented as a fix package of LAMMPS. An additional potential energy from the volume constraint is modeled as following:

$$H_v=\Lambda\left(\sum_k \Omega_k - V_{ref}\right)^2 \tag{C1}$$

where Ω_k is the signed volume of the tetrahedron extended by k-th triangle on the membrane, V_{ref} is the reference volume of the membrane and Λ is the Lagrange multiplier. Then, taking derivatives of the above potential with respect to each vertex gives the constraint forces from the volume constraint. For example, consider a triangle consists of three vertices: $\mathbf{r}_1, \mathbf{r}_2, \mathbf{r}_3$. The signed volume of the tetrahedron extended by this triangle is:

$$\Omega_k = \frac{1}{6}\mathbf{r}_1 \cdot \mathbf{r}_2 \times \mathbf{r}_3 \tag{C2}$$

Then, taking derivatives of Ω_k with respect to $\mathbf{r}_1$ is

$$\boldsymbol{\nabla}\Omega_k|_{\mathbf{r}_1} = \frac{1}{6}(-y_3z_2 + y_2z_3, x_3z_2 - x_2z_3, -x_3y_2 + x_2y_3) \tag{C3}$$

Other cases are cyclic permutations of the above result. Note that the interaction from the volume constraint is not pair-like interaction and total constraint force of vertex i is:

$$f^{(i)}_{constraint} = 2\Lambda \sum_{k\in\text{neighbors of i}} \boldsymbol{\nabla}\Omega_k|_{\mathbf{r}_i} \tag{C4}$$

Appendix D: Computation of curvatures

Computation of curvatures generally requires a surface is differentiable. However, in the discretization limit, the surface is composed of flat triangles and is a piece-wise constant surface, which has only C^0 continuity. Then, computation of curvatures on the triangulated surface needs additional considerations.

The method used in this paper to compute the curvatures of the magnetoelastic membranes follows the work of Meyer et al[45], which is introduced in the context of computer graphics. By associating each vertex with its corresponding Voronoi cell, the mean curvature vector $\mathbf{K}$ and the gaussian curvature κ_G are calculated by following formulae:

$$\mathbf{K}(\mathbf{r}_i) = \frac{1}{2A(\mathbf{r}_i)} \sum_{j\in\text{neighbors of i}} (\cot\alpha_{ij} + \cot\beta_{ij})(\mathbf{r}_i - \mathbf{r}_j) \tag{D1}$$

$$\kappa_G(\mathbf{r}_i) = \left(2\pi - \sum_{j\in\text{external angles}} \theta_j\right)/A(\mathbf{r}_i) \tag{D2}$$

where α_{ij} and β_{ij} are two angles opposite to the edge defined by vertices $\mathbf{r}_i$ and $\mathbf{r}_j$. $A(\mathbf{r}_i)$ is the area of Voronoi cell of vertex i:

$$A(\mathbf{r}_i) = \frac{1}{8} \sum_{j\in\text{neighbors of i}} (\cot\alpha_{ij} + \cot\beta_{ij})|\mathbf{r}_i - \mathbf{r}_j|^2 \tag{D3}$$

and θ_j are the external angles of the Voronoi cell around vertex i. Note that when triangles are obtuse, $A(\mathbf{r}_i)$ needs to be modified[45] to make sure that Voronoi cells are non-overlapping, which in turn makes sure that the sum of Gaussian curvature fulfills the Gauss-Bonnet theorem. By comparing the direction of mean curvature vector $\mathbf{K}$ with the exterior normal direction of the membrane, a sign can be associated with the mean curvature value to distinguish convex and concave regions of the membrane.

Appendix E: Membrane morphologies with the volume constraint

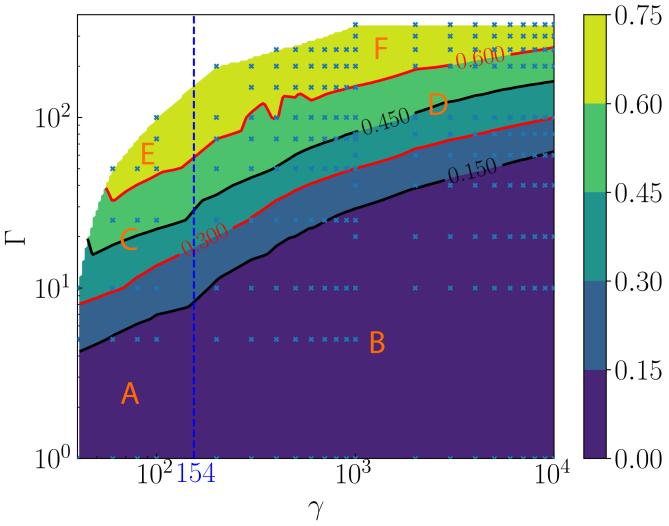

FIG. 4. A shape diagram for the closed homogeneous magnetoelastic crystalline membranes with the volume constraint. γ is the Föppl-von Kármán parameter and Γ is the magnetoelastic parameter. Blue crosses represent data points from simulations. Colors represent the magnetic energy contribution χ_m. Blue vertical dash line indicates the elastic buckling transition point and two red contour lines (30% and 60%) indicate estimations of magnetically induced membrane morphologies transition points. Different regions in the shape diagram correspond to different membrane morphologies: A. spheres; B. icosahedra; C. ellipsoids; D. star shapes with six ridges; E. cylinders; F. star shapes with four ridges;

Possible membrane morphologies with the volume constraint are presented in Fig. 2. Here we provide a more detailed analysis of membrane morphologies in terms of the energy competition between elastic and magnetic energy (Fig. 4). Simulations with different dimensionless parameters (γ, Γ) are represented by blue cross symbols in Fig. 4. Colors are obtained by the linear interpretation based on simulation data points, which represent the magnetic energy contributions. The magnetic energy contribution χ_m is defined as:

$$\chi_m = \frac{|H_m|}{|H_m| + H_e} \tag{E1}$$

where H_m and H_e are the total magnetic energy and elastic energy respectively. Based on the magnetic en-

ergy contributions, two red contour lines ($\sim$ 30% and $\sim$ 60%) are drawn to indicate estimated magnetically induced membrane morphologies transition points. Combining with the elastic buckling transition point $\gamma^* \sim 154$ (blue vertical dash line), the phase space of the system is roughly divided into regions which correspond to different possible membrane morphologies. Below the elastic buckling transition point($\gamma < \gamma^*$), the membrane morphologies change from spherical shapes(region A), to ellipsoidal shapes(region C) and to cylindrical shapes(region E) with increasing magnetoelastic parameter Γ. Above the elastic buckling transition point($\gamma > \gamma^*$), membrane morphologies change from icosahedral shapes (region B), to star shapes with six ridges (region D) and to star shapes with four ridges (region F) with increasing magnetoelastic parameter Γ. Blank regions correspond to an extremely strong magnetic field strength limit, where membrane morphologies are generally two-fold symmetric or collapsed.

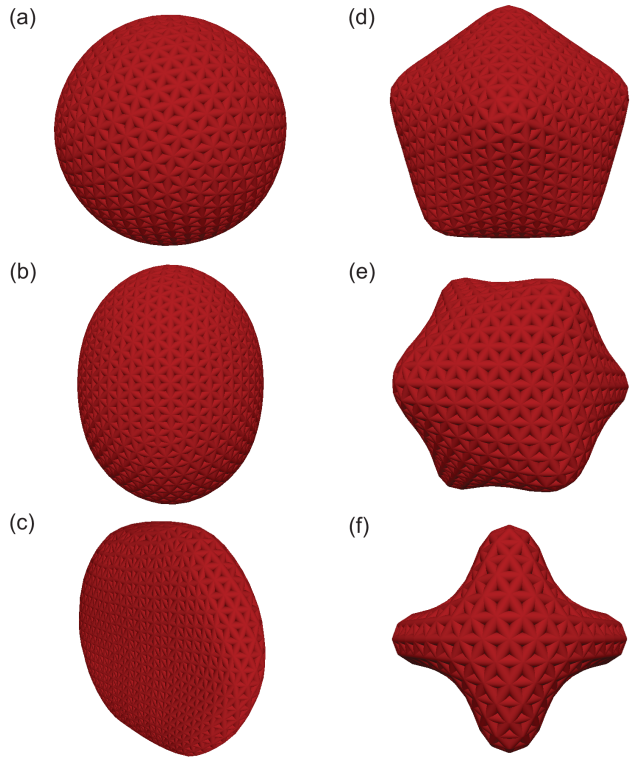

FIG. 5. A collection of representative minimum energy morphologies of the closed magnetoelastic membrane without the volume constraint. Different parameters pairs (γ, Γ), Föppl-von Kármán parameter γ and magnetoelastic parameter Γ, are explored. γ increases from left to right and Γ increases from top to bottom. (a) spherical shape (100,0); (b) icosahedral shape (1000,0); (c) ellipsoidal shape (100,20); (d) star shape with six ridges (1000,80); (e) pancake shape (100,40); (f) star shape with four ridges (1000,150). Note that (a) and (c) are shown from y-direction, (e) is shown in angled view and second column is shown from z-direction to give better illustration of morphologies.

Appendix F: Membrane morphologies without the volume constraint

We also explore cases without the volume constraint, which correspond to the situation that materials inside the membrane can freely penetrate the membrane. Possible morphologies of the membranes without the volume constraint are shown in Fig. 5.
When compared to the results with the volume constraint, the volume constraint shifts the transition points between different morphologies, which is expected and controlled by the parameters V_{ref} and Λ. The morphologies without the volume constraint generally do not differ significantly from cases with the volume constraint, except in cases with a high magnetic field strength.

For example, as shown in Fig. 5e, the membrane morphology becomes "pancake" shape when the membrane is relatively soft ($\gamma < \gamma^*$) in the high field strength limit. The "pancake" shape brings magnetic dipoles even closer than cylindrical shape(Fig. 2e) since there is no additional volume constraint to prevent the membrane from shrinking.

When the membrane is relatively stiff ($\gamma > \gamma^*$) in the high field strength limit, many crumpled states or collapsed states are observed as shown in Fig. 6. These morphologies are difficult to describe and generally differ a lot from each other. The magnetoelastic membranes in those cases are highly nonlinear and both magnetic and elastic energy are important. Small fluctuations of the membrane disclinations can change the membrane morphology significantly in those cases and lead to different crumpled states or collapsed states. Without the vol-

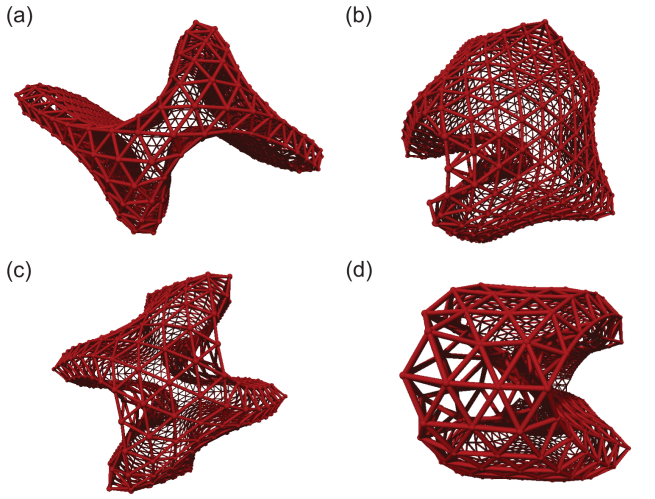

FIG. 6. Examples of crumpled states and collapsed states. These morphologies are observed in the cases without the volume constraint in the high magnetic field strength limit. Their corresponding parameters pairs (γ, Γ) are: (a) (2000,600); (b) (4000,200); (c) (6000,500); (d) (8000, 400). All of them are shown from z-direction and are represented by triangulation meshes to show overlapping regions.

ume constraint, the membranes resist magnetic dipole-dipole interactions by elasticity(although Lennard-Jones interactions also help stabilizing the membrane when the membrane is collapsed). After reaching a certain magnetic field strength, the membranes cannot hold a definite shape anymore and are free to crumple or collapse since there is no volume constraint to restrict these crumpling or collapsing processes. This creates a family of complicated morphologies, which are strongly deformed. Selected representative crumpled and collapsed morphologies shown in Fig. 6 are repeated with finer mesh size (up to mesh (12,12) which has 4322 vertices) to ensure that these morphologies do not result from insufficient discretization. It is interesting to notice that these morphologies in Fig. 6 ($\gamma > \gamma^*$ in high magnetic field strength limit), still roughly maintain two-fold symmetry for some states (Fig. 6a, c, and d).

[1] H. W. Kroto, J. R. Heath, S. C. O'Brien, R. F. Curl, and R. E. Smalley. C60: Buckminsterfullerene. *Nature*, 318(6042):162–163, 1985.

[2] Chenguang Fan, Shouqiang Cheng, Yu Liu, Cristina M. Escobar, Christopher S. Crowley, Robert E. Jefferson, Todd O. Yeates, and Thomas A. Bobik. Short n-terminal sequences package proteins into bacterial microcompartments. *Proceedings of the National Academy of Sciences*, 107(16):7509, 2010.

[3] C. I. Zoldesi, I. L. Ivanovska, C. Quilliet, G. J. L. Wuite, and A. Imhof. Elastic properties of hollow colloidal particles. *Phys. Rev. E*, 78:051401, 2008.

[4] Carmen I. Zoldesi, Cornelis A. van Walree, and Arnout Imhof. Deformable hollow hybrid silica/siloxane colloids by emulsion templating. *Langmuir*, 22(9), 2006.

[5] Jissy Jose, Marlous Kamp, Alfons van Blaaderen, and Arnout Imhof. Unloading and reloading colloidal microcapsules with apolar solutions by controlled and reversible buckling. *Langmuir*, 30(9):2385–2393, 2014.

[6] Jack Lidmar, Leonid Mirny, and David R. Nelson. Virus shapes and buckling transitions in spherical shells. *Phys. Rev. E*, 68:051910, 2003.

[7] Siyu Li, Polly Roy, Alex Travesset, and Roya Zandi. Why large icosahedral viruses need scaffolding proteins. *Proceedings of the National Academy of Sciences*, 115(43):10971, 2018.

[8] Edward J. Banigan, Andrew D. Stephens, and John F. Marko. Mechanics and buckling of biopolymeric shells and cell nuclei. *Biophysical Journal*, 113(8):1654–1663, 2017.

[9] Maxim O. Lavrentovich, Eric M. Horsley, Asja Radja, Alison M. Sweeney, and Randall D. Kamien. First-order patterning transitions on a sphere as a route to cell morphology. *Proceedings of the National Academy of Sciences*, 113(19):5189, 2016.

[10] Eric Raspaud, Bruno Pitard, Dominique Durand, Olivier Aguerre-Chariol, Juan Pelta, Gerardo Byk, Daniel Scherman, and Franoise Livolant. Polymorphism of dna/multicationic lipid complexes driven by temperature and salts. *J. Phys. Chem. B*, 105(22):5291–5297, 2001.

[11] Graziano Vernizzi and Monica Olvera de la Cruz. Faceting ionic shells into icosahedra via electrostatics. *Proceedings of the National Academy of Sciences*, 104(47):18382, 2007.

[12] Y. Chushak and A. Travesset. Solid domains in lipid vesicles and scars. *Europhysics Letters*, 72(5):767–773, 2005.

[13] Franois Quemeneur, Catherine Quilliet, Magalie Faivre, Annie Viallat, and Brigitte Ppin-Donat. Gel phase vesicles buckle into specific shapes. *Phys. Rev. Lett.*, 108(10):108303, 2012.

[14] Sebastian Knoche and Jan Kierfeld. Buckling of spherical capsules. *Phys. Rev. E*, 84(4), 2011.

[15] Sujit S. Datta, Shin-Hyun Kim, Jayson Paulose, Alireza Abbaspourrad, David R. Nelson, and David A. Weitz. Delayed buckling and guided folding of inhomogeneous capsules. *Phys. Rev. Lett.*, 109:134302, 2012.

[16] G. A. Vliegenthart and G. Gompper. Compression, crumpling and collapse of spherical shells and capsules. *New Journal of Physics*, 13(4):045020, 2011.

[17] Roya Zandi, David Reguera, Robijn F. Bruinsma, William M. Gelbart, and Joseph Rudnick. Origin of icosahedral symmetry in viruses. *Proceedings of the National Academy of Sciences*, 101(44):15556, 2004.

[18] H. S. Seung and David R. Nelson. Defects in flexible membranes with crystalline order. *Phys. Rev. A*, 38:1005–1018, 1988.

[19] Graziano Vernizzi, Rastko Sknepnek, and Monica Olvera de la Cruz. Platonic and archimedean geometries in multicomponent elastic membranes. *Proceedings of the National Academy of Sciences*, 108(11):4292–4296, 2011.

[20] Ee Hou Yong, David R. Nelson, and L. Mahadevan. Elastic platonic shells. *Phys. Rev. Lett.*, 111:177801, 2013.

[21] Simona Mura, Julien Nicolas, and Patrick Couvreur. Stimuli-responsive nanocarriers for drug delivery. *Nature Materials*, 12:991, 2013.

[22] Theresa M. Allen and Pieter R. Cullis. Liposomal drug delivery systems: From concept to clinical applications. *Advanced Drug Delivery Reviews*, 65(1):36–48, 2013.

[23] Hang Xing, Kevin Hwang, and Yi Lu. Recent developments of liposomes as nanocarriers for theranostic applications. *Theranostics*, 6(9):1336, 2016.

[24] Vikas Nandwana, Abhalaxmi Singh, Marisa M. You, Gefei Zhang, John Higham, Tiffany S. Zheng, Yue Li, Pottumarthi V. Prasad, and Vinayak P. Dravid. Magnetic lipid nanocapsules (mlncs): self-assembled lipid-based nanoconstruct for non-invasive theranostic applications. *J. Mater. Chem. B*, 6:1026–1034, 2018.

[25] Yoonho Kim, Hyunwoo Yuk, Ruike Zhao, Shawn A. Chester, and Xuanhe Zhao. Printing ferromagnetic domains for untethered fast-transforming soft materials. *Nature*, 558(7709):274–279, 2018.

[26] Guo Zhan Lum, Zhou Ye, Xiaoguang Dong, Hamid Marvi, Onder Erin, Wenqi Hu, and Metin Sitti. Shape-programmable magnetic soft matter. *Proceedings of the National Academy of Sciences*, 113(41):E6007–E6015, 2016.

[27] Wenqi Hu, Guo Zhan Lum, Massimo Mastrangeli, and Metin Sitti. Small-scale soft-bodied robot with multimodal locomotion. *Nature*, 554:81, 2018.

[28] Chase Austyn Brisbois, Mykola Tasinkevych, Pablo Vzquez-Montejo, and Monica Olvera de la Cruz. Actuation of magnetoelastic membranes in precessing magnetic fields. *Proceedings of the National Academy of Sciences*, 116(7):2500, 2019.

[29] Rmi Dreyfus, Jean Baudry, Marcus L. Roper, Marc Fermigier, Howard A. Stone, and Jrme Bibette. Microscopic artificial swimmers. *Nature*, 437:862, 2005.

[30] Hui Wang, Yifei Yu, Yubin Sun, and Qianwang Chen. Magnetic nanochains: a review. *Nano*, 06(01):1–17, 2011.

[31] Jiachen Wei, Fan Song, and Jure Dobnikar. Assembly of superparamagnetic filaments in external field. *Langmuir*, 32(36):9321–9328, 2016.

[32] Joshua M. Dempster, Pablo Vázquez-Montejo, and Monica Olvera de la Cruz. Contractile actuation and dynamical gel assembly of paramagnetic filaments in fast precessing fields. *Phys. Rev. E*, 95:052606, 2017.

[33] Pablo Vázquez-Montejo, Joshua M. Dempster, and Mónica Olvera de la Cruz. Paramagnetic filaments in a fast precessing field: Planar versus helical conformations. *Phys. Rev. Materials*, 1:064402, 2017.

[34] Mark J. Bowick, David R. Nelson, and Alex Travesset. Interacting topological defects on frozen topographies. *Phys. Rev. B*, 62:8738–8751, 2000.

[35] D. L. D. Caspar and A. Klug. Physical principles in the construction of regular viruses. *Cold Spring Harbor Symposia on Quantitative Biology*, 27:1–24, 1962.

[36] G. Gompper and D. M. Kroll. Random surface discretizations and the renormalization of the bending rigidity. *J. Phys. I France*, 6(10):1305–1320, 1996.

[37] D. R. Nelson, T. Piran, and S. Weinberg. *Statistical Mechanics of Membranes and Surfaces*. World Scientific Pub., 2004.

[38] A. Libai and J.G. Simmonds. *The Nonlinear Theory of Elastic Shells*. Cambridge University Press, 1998.

[39] Pablo Vázquez-Montejo and Mónica Olvera de la Cruz. Flexible paramagnetic membranes in fast precessing fields. *Phys. Rev. E*, 98:032603, 2018.

[40] T. A. Witten. Stress focusing in elastic sheets. *Rev. Mod. Phys.*, 79:643–675, 2007.

[41] Alex Lobkovsky, Sharon Gentges, Hao Li, David Morse, and T. A. Witten. Scaling properties of stretching ridges in a crumpled elastic sheet. *Science*, 270(5241):1482, 1995.

[42] Alexander E. Lobkovsky and T. A. Witten. Properties of ridges in elastic membranes. *Phys. Rev. E*, 55:1577–1589, 1997.

[43] B. A. DiDonna and T. A. Witten. Anomalous strength of membranes with elastic ridges. *Phys. Rev. Lett.*, 87:206105, 2001.

[44] Steve Plimpton. Fast parallel algorithms for short-range molecular dynamics. *Journal of Computational Physics*, 117(1):1–19, 1995.

[45] Mark Meyer, Mathieu Desbrun, Peter Schrder, and Alan H. Barr. Discrete differential-geometry operators for triangulated 2-manifolds. In *Visualization and Mathematics III*, pages 35–57, 2003.